ACS APPLIED MATERIALS & INTERFACES

www.acsami.org

Research Article

Thermodynamic and Transport Properties of LiF and FLiBe Molten Salts with Deep Learning Potentials

Alejandro Rodriguez,* Stephen Lam, and Ming Hu

Cite This: *ACS Appl. Mater. Interfaces* 2021, 13, 55367−55379

Read Online

ACCESS | Metrics & More | Article Recommendations

ABSTRACT: Molten salts have attracted interest as potential heat carriers and/or fuel solvents in the development of new Gen IV nuclear reactor designs, high-temperature batteries, and thermal energy storage. In nuclear engineering, salts containing lithium fluoride-based compounds are of particular interest due to their ability to lower the melting points of mixtures and their compatibility with alloys. A machine learning potential (MLP) combined with a molecular dynamics study is performed on two popular molten salts, namely, LiF (50% Li) and FLiBe (66% LiF and 33% BeF_2), to predict the thermodynamic and transport properties, such as density, diffusion coefficients, thermal conductivity, electrical conductivity, and shear viscosity. Due to the large possibilities of atomic environments, we employ training using Deep Potential Smooth Edition (DPSE) neural networks to learn from large datasets of 141,278 structures with 70 atoms for LiF and 238,610 structures with 91 atoms for FLiBe molten salts. These networks are then deployed in fast molecular dynamics to predict the thermodynamic and transport properties that are only accessible at longer time scales and are otherwise difficult to calculate with classical potentials, *ab initio* molecular dynamics, or experiments. The prospect of this work is to provide guidance for future works to develop general MLPs for high-throughput thermophysical database generation for a wide spectrum of molten salts.

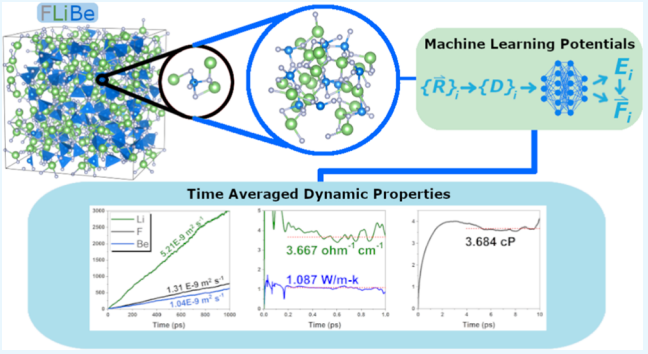

KEYWORDS: *machine learning, interatomic potential, molten salt, thermodynamics, molecular dynamics*

1. INTRODUCTION

Molten salt reactors (MSRs) first appeared in the mid-20th century and have recently been accepted as candidate Gen IV reactors competing with the existing light water and boiling water reactors.[1−3] The design of MSRs centralizes molten salts as fuels and heat carriers in the primary loop, providing inherent advantages over commercial technologies such as meltdown mitigation through passive cooling, negative temperature coefficients of reactivity, low operating pressures, increased operating temperatures for efficiency, and improved waste management.[4,5] However, as molten salts are required to satisfy a diverse number of nuclear, physical, and chemical criteria to operate effectively, knowledge on salt properties is essential for MSR design.[6,7] So far, thermodynamic and thermophysical databases for molten salts are limited by the difficulty of high temperature, toxicity, and corrosive experiments.[8,9] Furthermore, the possible number of salt configurations, including single, binary, ternary, and more complex mixtures of compounds, with the consideration of impurities from chromium alloys and other particulates, further increases the design space of MSRs. This huge design space calls for the development of theoretical and/or computational methods to speed up the present bottlenecks in experimental methods.

In recent years, computational simulations of candidate MSR fuels permitted a deeper understanding of their behavior and structure. Salanne et al. developed the polarizable interaction potential (PIM) to study ionic liquids by inclusion of polarization effects, which has been used to study a wide variety of single and binary molten salts involving LiF, NaF, KF, BeF_2, and ThF_4 end members with high accuracy relative to experiment.[10−16] Nam et al. studied the structural effects of chromium dissolved in FLiBe and FLiNaK melts using *ab initio* molecular dynamics (AIMD) to observe chromium fluoride formations and diffusivity as a function of chromium valence.[17] Similarly, Lam et al. studied FLiBe and FLiNaK with AIMD to observe tritium complexes and diffusivity.[18] However, the costly performance of *ab initio* methods with system size creates difficulty when predicting properties where long time scale statistics are needed, and the a priori nature of classical

Received: September 16, 2021
Accepted: November 4, 2021
Published: November 12, 2021

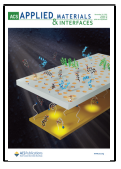

https://doi.org/10.1021/acsami.1c17942
ACS Appl. Mater. Interfaces 2021, 13, 55367−55379

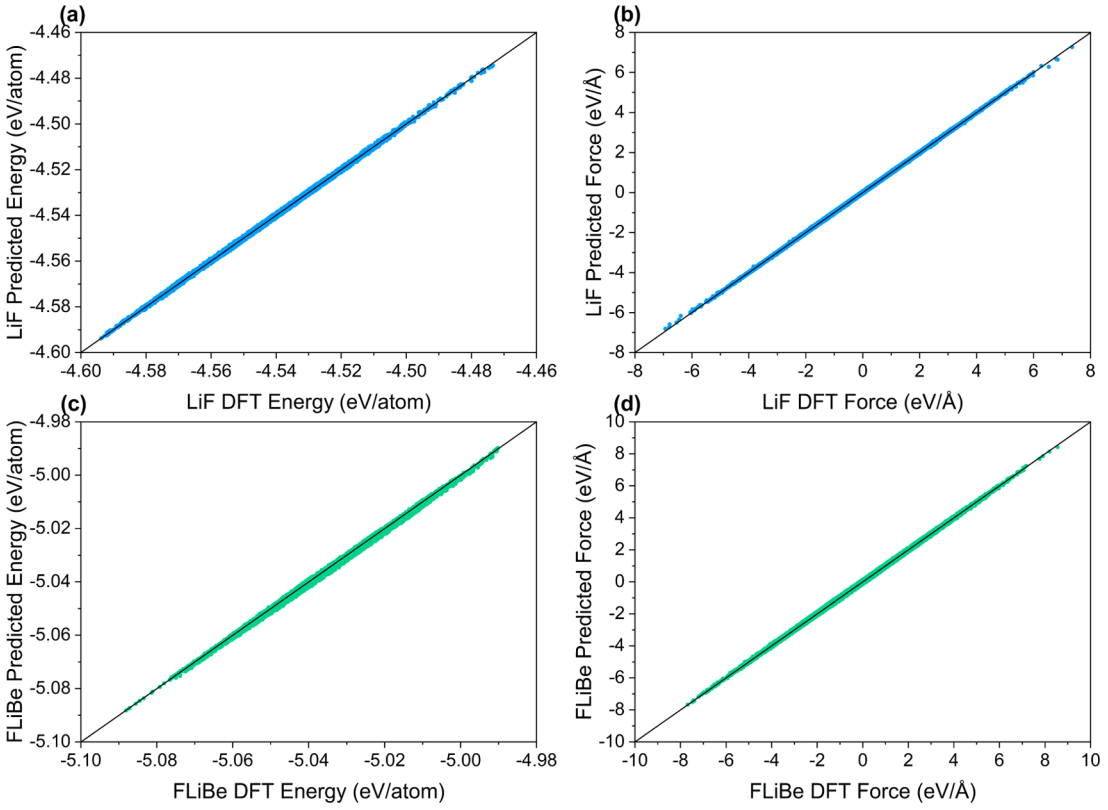

Figure 1. Plots comparing unobserved testing DFT and DeePMD predictions for (a) LiF energy and (b) forces and (c) FLiBe energy and (d) forces. Results closer to unity are better, and the black line is to guide the eyes.

potentials such as PIM requires the re-fitting of new potentials when encountering new end members and/or elemental impurities in the system. Recently, a new class of potentials called the machine learning potential (MLP) allow researchers to approach materials with an "out-of-the-box" mindset when compared to classical potentials, requiring no knowledge of the mathematical form of the potential for a particular material. Further, MLPs can reduce the severity of cost accuracy trade-off associated with classical potentials by finding more optimal functions for describing the interatomic interactions in systems of high complexity (structural, compositional, and chemical). Recently, LiF and FLiBe salts have been studied using a neural network-based MLP for the equation of state, surface energies, local structure, and self-diffusivity,[19] but no works have been published that predict the transport properties of molten salts with MLPs to the best of our knowledge.

In this paper, we train an MLP using the Deep Potential Molecular Dynamics (DeePMD) method to model the transport properties of the single salt lithium fluoride (LiF) and the binary salt FLiBe (66% LiF and 33% BeF_2).[20] While the previous paper by Lam utilized a modified Behler–Parrinello descriptor, we chose DeePMD for its reduced manual input in hyper-parameterization. The model requires only the finite distance cutoff and the maximum number of neighbors found in the dataset. This is a critical feature for general modeling of molten salts, considering the complex and diverse local complexes formed in melts such as BeF_4^{2-} tetrahedral and polymer-like chains in denser compositions.[21] In addition, we validate the results of the training by evaluation of transport properties as functions of temperature. It is well known that the transport properties of molten salts are the most difficult to evaluate both experimentally and theoretically,[10,22−25] and from our knowledge, no other works have evaluated the transport properties of molten salts with MLPs. In Section 2, we cover the development of LiF and FLiBe DeePMD potentials, including details on dataset generation, training, and MD. Section 3 details the various properties predicted from the DeepMD-Smooth Edition (DPSE) potential and compares them to other works including experimental and MD results. Finally, Section 4 concludes this work with a brief discussion on our future work concerning molten salt modeling.

2. COMPUTATIONAL DETAILS

2.1. Dataset Generation. Training for LiF and FLiBe neural network potentials requires a dataset that sufficiently covers the range of configurations that may manifest during finite-temperature MD simulations. As such, data for LiF and FLiBe configurations were borrowed from the existing *ab initio* MD data with simulation details previously described.[19] Briefly, calculations were performed using the Vienna Ab Initio Simulation Package (VASP) with the plane wave basis set and periodic boundary conditions in all cell directions. The plane wave energy cutoff is 600 eV, and the k-point sampling is done on a 2 × 2 × 2 Γ-centered grid. All calculations were performed using the Perdew–Burke–Ernzerhof (PBE) generalized gradient approximation exchange–correlation functional and projector-augmented wave potentials. The LiF dataset contains 118,115 configurations with 70 atom supercells at 1200 K and experimental density, and the FLiBe dataset contains 222,903 configurations with 91 atom supercells at 973 K and experimental density. To capture changes in volume, we also generated a mixed dataset containing −5, 1, 5, and 10% changes to the lattice constant for 9208, 3951, 5253, and 4751

https://doi.org/10.1021/acsami.1c17942
ACS Appl. Mater. Interfaces 2021, 13, 55367−55379

(23,163 total) LiF configurations, respectively, and 7168, 1188, 4017, and 3334 (15,707 total) FLiBe configurations, respectively, with all systems under the same simulation parameters and conditions. With the LiF and FLiBe datasets, each was shuffled and split 80−20% for training and testing.

2.2. Atomic Potential Training. For training an atomic potential, we opted for the DeePMD-kit (DP-kit) package, a Python/C++ package for neural network training and evaluation of atomic energies and forces with efficient tensor operations through the Tensorflow interface.[26,27] The Deep-Pot-Smooth Edition (DPSE) potential contained inside the above package is chosen due to its natural symmetry conservation of atomic descriptors.[28] Here, the smooth cutoff and hard cutoff distance was chosen as 2 and 7 Å, respectively. The choice of hard cutoff is primarily due to the time savings in FLiBe MD (1.3187×10^{-3} time/step/atom for 7 Å vs 2.3187×10^{-3} time/step/atom for 9 Å) with a negligible 0.03 g/cm^3 improvement in the predicted density, whereas the smooth cutoff from 8.8 to 2 Å shows an ∼0.01 g/cm^3 improvement with no notable difference in speed. The resulting training of DPSE networks yielded a testing root-mean-squared error of 2.54×10^{-5} eV/atom and 13.8 meV/Å for LiF energy and forces, respectively, and 4.86×10^{-5} eV/atom and 23.2 meV/Å for FLiBe energy and forces, respectively. As exhibited by the comparison of the testing energies and forces in Figure 1, the excellent accuracy on untrained data suggests well-represented potentials for simulating *ab initio* potential energy surfaces and ensuing dynamics for LiF and FLiBe molten salts.

To generate acceptable MLPs with high quality of energy and force, sufficient data must be provided during training to capture, at minimum, a range of all possible configurations that may be found during finite-temperature MD simulations. Due to the costly nature of *ab initio* calculations, it is of interest to minimize the computational cost from the data generation step by requiring the least number of configurations needed for converged force and energy testing errors, such that any further training is not necessary to sufficiently generalize the unseen structures. We have provided Figure 2 which contains both energy and force errors against the number of AIMD steps. From our existing FLiBe data, 50,000 constant volume AIMD steps were isolated as training data, leaving the remaining 172,903 structures for testing. We further split the training data into segments and train various models with increasing number of steps, each inheriting the same data as the last. After training, we evaluate the same testing set with the models and compare the model output with *ab initio* energies and forces. As can be seen from the figure, acceptable RMSE values are reached around 10,000 steps, with slight fluctuations in the force and energy RMSE thereafter.

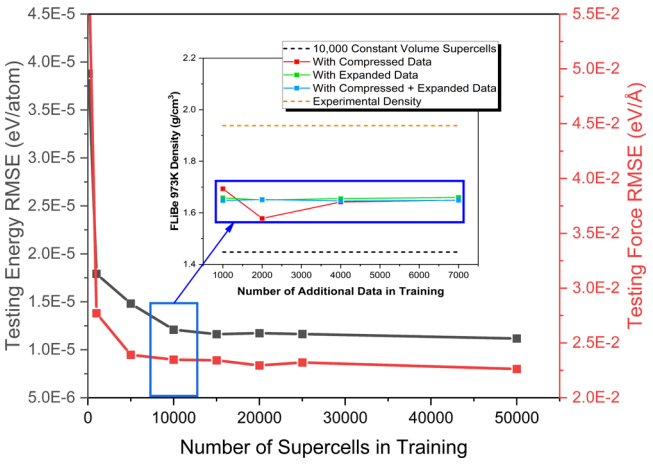

Figure 2. Energy and force RMSE for FLiBe against the number of supercells used in training. Inset: the resulting density of DPSE simulations versus the number of additional volume data in the 10,000 constant volume dataset for training.

Furthermore, the effect of compressed/expanded volume data on model accuracy is investigated. Provided the converged model at 10,000 constant volume configurations, we re-train new models with the same previous 10,000 steps but with the existing variable volume data, such that 1000, 2000, 4000, and 7000 compressed, expanded, and 50/50 compressed/expanded volume data are included for training (*i.e.*, yielding 12 new networks). We then evaluate the same testing set as before to find the RMSE. Note that the expanded volume data is randomly selected from the pool of +1, +5, and +10% lattice constant datasets. From our training of additional volumes, all force RMSE values lie on the converged 23.5 meV/Å found from constant volume networks, while the energy RMSE fluctuates about 3×10^{-5} eV/atom, more than double the 1.21×10^{-5} eV/atom in the constant volume case. Although an energy RMSE increase is observed with added volume data, we emphasize this as a necessary trade-off to improve the quality of molten salt MD simulations due to the improvement of the predicted density and subsequent properties as discussed in Section 3. A. The networks trained with a constant volume either resulted in very low or unstable densities in which excessive cell expansion occurs, with no particular pattern in the increasing number of constant volume configurations. Here, we briefly show how the inclusion of variable volumes improves the resulting density *via* MD simulations with the aforementioned DPSE models. The setup for MD is described in Section 2.3. The inset of Figure 2 shows a 10.4% improvement to the predicted density at 973 K with additional volume data. Interestingly, all networks including expanded data seem to converge with only 1000 additional structures (500 expanded structures in the compressed + expanded case), whereas the pure compression case requires at least 4000 to reach a similar density. We assign the performance increase by the inclusion of forces in an expanded system, with the DPSE model more accurately capturing the calculated pressure under cell expansion and converging to a relatively higher density. On the other hand, without the expanded data, the pure compressed case requires more samples to reach density convergence. We theorize that the compressed system improves the quality of short-ranged interactions and promotes the attractive potential between atoms in the system.

2.3. Molecular Dynamics. After training on the dataset, the DPSE potentials were used in the Large Scale Atomic/Molecular Massively Parallel Simulator (LAMMPS) *via* the interface with DeePMD-kit.[29] Specifically, a pair style in LAMMPS uses the trained model for energy and force calculation during MD steps. Exploiting the linear scaling of DPSE, the supercell from AIMD is extended to a 2 × 2 × 2 system as the initial structure, resulting in 560 LiF atoms and 728 FLiBe atoms. The temperature was chosen such that the system is well beyond its liquidus; thus, the systems are simulated at 1120−1320 K at 40 K intervals for LiF and 800−1100 K at 100 K intervals +973 K for FLiBe. With 1 fs as the time step, the system is first relaxed for 250 ps under *NVT*,

https://doi.org/10.1021/acsami.1c17942
ACS Appl. Mater. Interfaces 2021, 13, 55367−55379

followed by 250 ps under *NPT*, where the lattice constant is taken from the average volume during *NPT*. Then, we perform two sets of production runs at various temperatures, one set using the calculated relaxed volumes and the other set at experimentally known densities. Both of these sets of simulations undergo 100 ps of *NVT*, followed by 1000 ps of *NVE*. We note that the temperature range of the MD simulations is outside the constant temperature simulations of the training dataset. Nonetheless, the structure of the melts does not vary strongly within the small temperature range as discussed in Section 3.2, and the current model was sufficient for our study.

To display the linear scaling of MLPs, we generated Figure 3 containing the CPU time per time step against the system size of LiF. As can be seen from the figure, the evaluation time for AIMD scales closely with the number of atoms cubed. On the other hand, the rigid ion model (RIM),[30,31] a parameterized potential, the spatial density neural network force field (SDNNFF),[32] a machine learning force field, and DPSE all scale linearly with the system size. Although the ML-based methods are more time-consuming in comparison to parameterized potentials, they offer the same linear scaling quality inaccessible by first-principles while representing the potential energy surfaces seen in DFT. Moreover, the computational cost of MLPs can be reduced by a constant if efforts are made to prune the model or systemically reduce the number of inputs to remove redundant or insignificant parameters, after the network has been trained. In this way, the MLP performance can be tuned based on the required sensitivity/accuracy of the system in a way that classical models cannot.

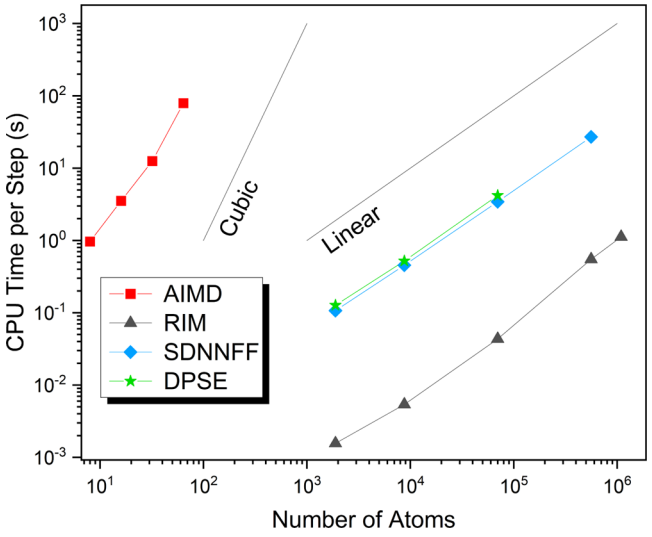

Figure 3. Time scaling of AIMD, RIM, SDNNFF, and DPSE against system size (lower is better).

3. THERMODYNAMIC AND TRANSPORT PROPERTIES

3.1. Density. For the determination of transport properties in MD, the density ρ of molten salts is closely related to the composition and existing local structures in the salt and is essential for matching subsequent properties with the experiment. Several studies on thermal conductivity through equilibrium MD simulations have shown direct correlation with the number density of the melt and cell volume.[16,33] Additionally, the model developed by Gheribi et al. for thermal conductivity prediction strongly depends on known densities of molten alkali and alkaline earth salts, with a relatively weak dependence on temperature.[22] As mentioned in the previous section, *NPT* relaxations on LiF and FLiBe were performed to obtain the equilibrium volumes from the DPSE potential, and the resulting densities versus temperature are plotted in Figure 4. As can be seen in the figure, the densities follow a similar downward trend as experiment but are ~14% lower when compared with the absolute value. We attribute the higher average volume to the quality of the DFT dataset the DPSE was trained on. A previous study by Nam et al. determined by

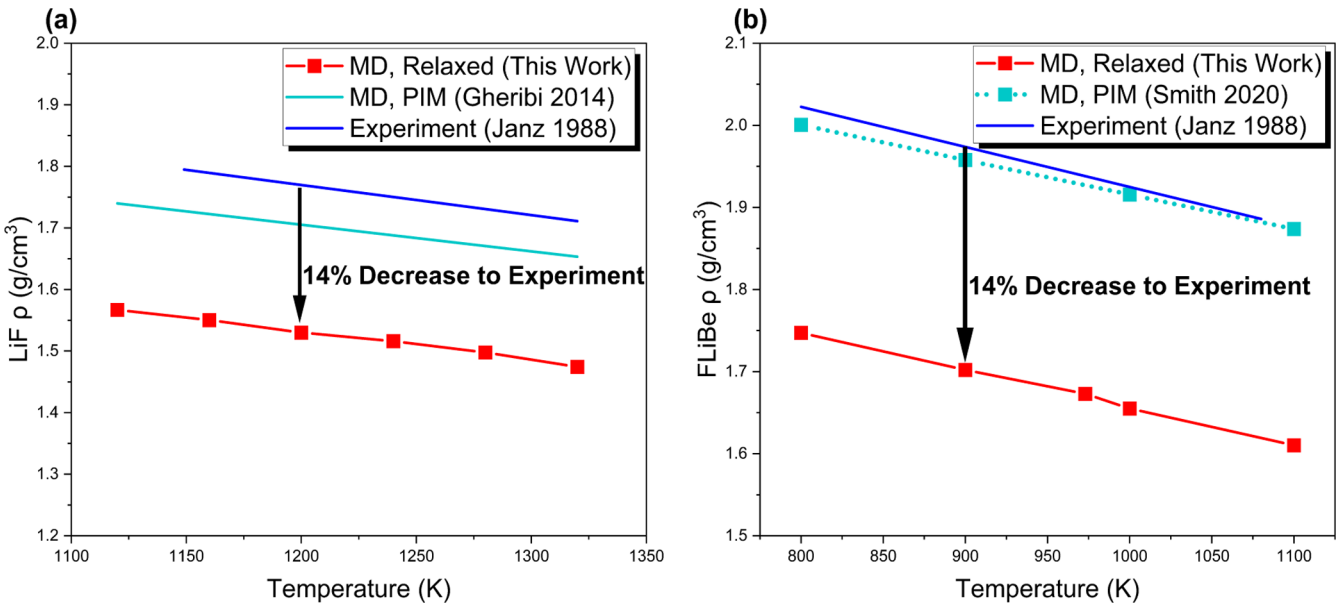

Figure 4. Plots of density against temperature for LiF and FLiBe above the melting point. (a) In order as shown in the legend, the density for LiF under NPT is obtained from our work, MD with the PIM model,[24] and experiment.[35] (b) Similarly, values for FLiBe under NPT from our work, MD with the PIM model,[36] and experiment are shown.[35]

https://doi.org/10.1021/acsami.1c17942
ACS Appl. Mater. Interfaces 2021, 13, 55367−55379

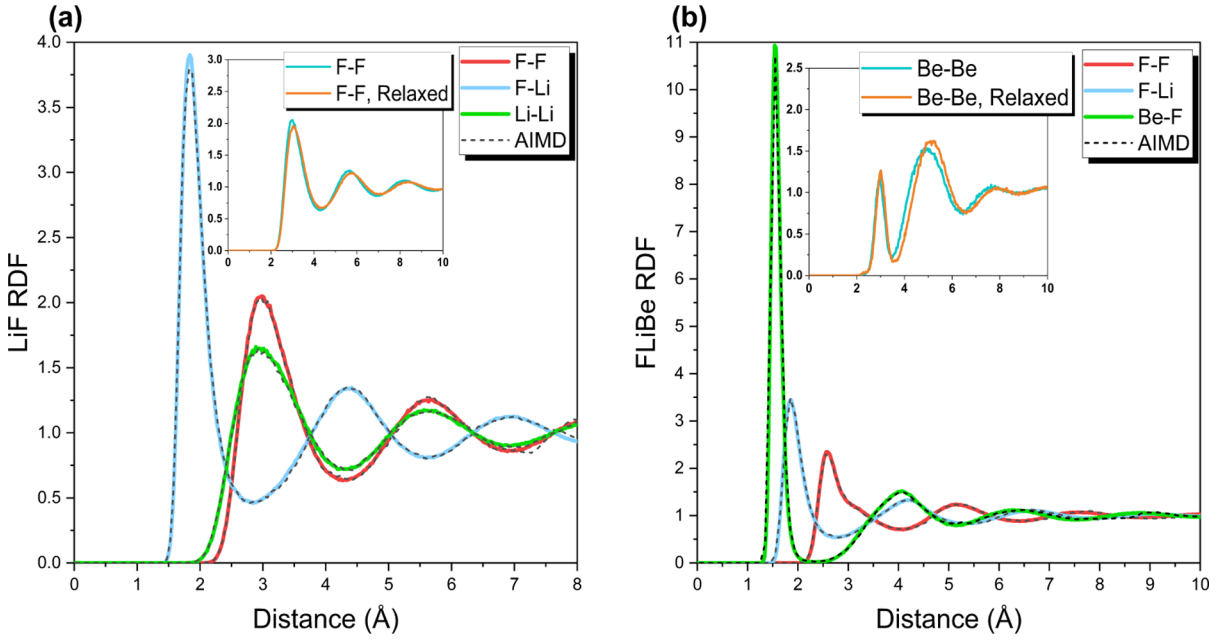

Figure 5. RDF curves for (a) LiF at 1200 K and (b) FLiBe at 973 K in comparison to AIMD. (Inset) RDF curves comparing like-charged ions with largest disagreement between MD relaxed and experimental densities.

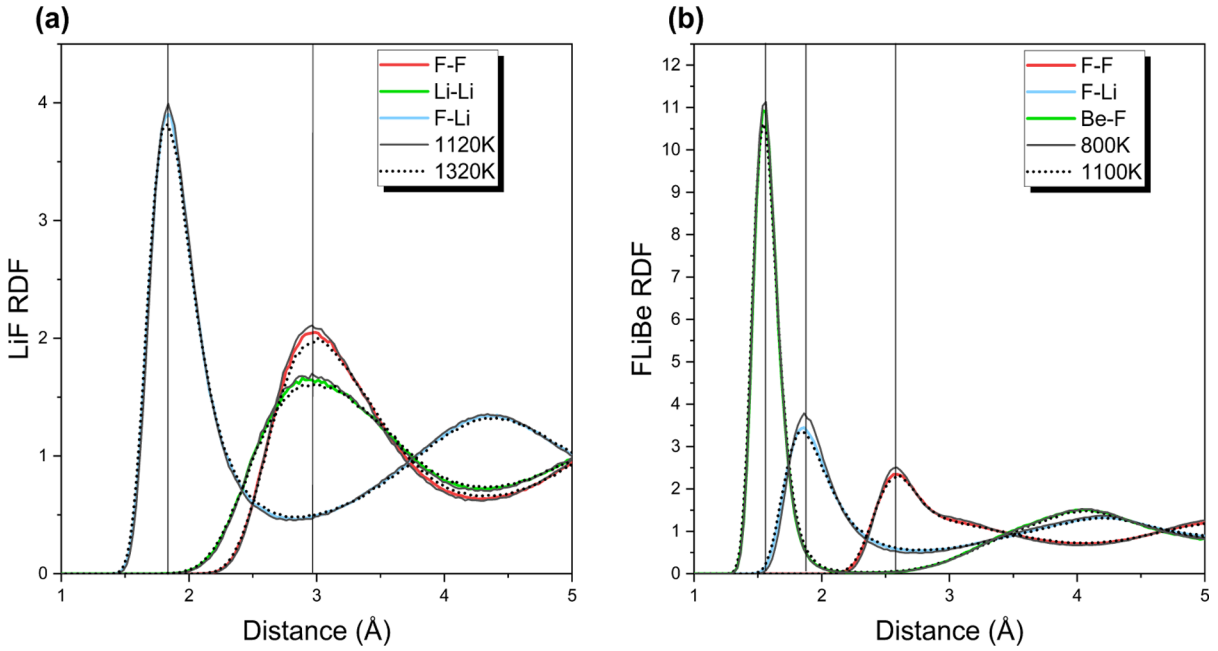

Figure 6. RDF curves against temperature for (a) LiF at 1200 K and (b) FLiBe at 973 K. Solid vertical lines guide the eyes for the first peak positions. Solid black curves represent the RDF at the lowest temperature here, while dotted curves are those at the highest temperature.

first-principles MD that the effect of van der Waals (vdW) on FLiBe volume is significant, such that no consideration of dispersion forces can lead to 18% higher volume with the PBE pseudopotential.[17] Although the addition of mixed volumes in the training set promotes higher density as can be seen in the inset of Figure 2, the resulting densities are still within the lower 10−20% region, which we attribute to the lack of dispersion interactions in the training data. Moreover, accurate inclusion of dispersion effects can be non-trivial. In standard deep neural network potentials and DeepMD, the distance cutoff results in truncation of long-range electrostatic and dispersion interactions. Recent efforts (third- and fourth-generation NNIPs) have sought to resolve this using additional neural networks to predict environment-dependent charges that can be used to predict long-range interactions.[34] For this work, we proceed to evaluate other transport properties in MD at both *NPT* relaxed volumes and experimental densities to emphasize the importance of capturing density, a relatively straightforward property to calculate, before computing complex transport properties, such as thermal conductivity. For future studies, we strongly suggest including vdW dispersion interactions such as vdW-DF or DFT-D2 in generating molten salt datasets from DFT since exchange−correlation functionals cannot consider these dispersion

https://doi.org/10.1021/acsami.1c17942
ACS Appl. Mater. Interfaces 2021, 13, 55367−55379

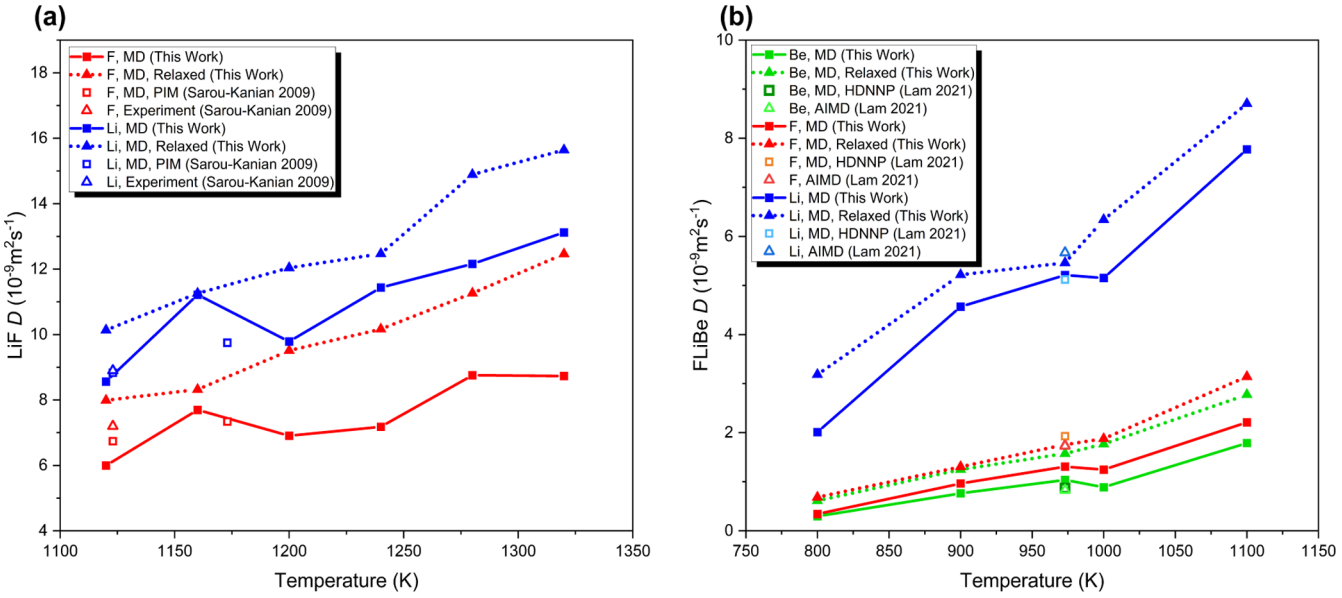

Figure 7. Plots of the diffusion coefficients against temperature for LiF and FLiBe above the melting point. (a) Diffusion coefficients for LiF at experimental and NPT relaxed volumes are obtained from our work, MD with the PIM model,[13] and experimental results.[13] (b) Diffusion coefficients for FLiBe at experimental and NPT relaxed volume are obtained from our work, MD with HDNNP,[19] and AIMD results.[19]

interactions on their own. Further, we recommend testing different neural network schemes for representing these interactions with high fidelity.

3.2. Radial Distribution Function. To measure the local structure of ionic fluids, the radial distribution function (RDF) and diffusion coefficients are compared between DPSE-MD, AIMD, and results from other papers. As can be seen from Figure 5, the RDF curves found from DPSE-MD match excellently with AIMD and confirm the efficacy of the potential. Furthermore, these curves for FLiBe and LiF offer insight into the decrease in density after MD relaxation. For the inset of Figure 5, only Be−Be RDF for the relaxed structure is compared with that from the experimental structure for brevity since the other RDF pairs show little variation in peak positions. As such, the drop in density is attributed to the expansion between Be−Be pairs, as noted by the stretched inter-peak distances for relaxed structures. This phenomenon has also been observed by Jabes et al. when comparing the transferable rigid ion model (TRIM) and polarizable ion model (PIM) atomic potentials for FLiBe, where lack of polarizability effects in the TRIM potential led to stretched Be−Be peaks and a reduction in density by 17−20%.[21] The expansion of RDF peaks is also observed for the LiF system as seen in the inset for Figure 5. Again, we isolated the F−F pair for brevity, which contains the largest discrepancy between relaxed and experimental volumes. A similar behavior is found as with the Be−Be pair for FLiBe, with relaxed LiF experiencing larger F−F peak distances, although the stretch is not as pronounced as that for the FLiBe Be−Be pair. Due to the shared volume expansion of both systems, the absence of dispersive interactions from AIMD results in a weak representation of the interactions between like-charged ions, which are essential for the precise modeling of local structures and the resulting density in molten salts.

To showcase the temperature dependence on the local structures of liquid LiF and FLiBe, Figure 6 plots RDF curves for various temperatures found from DPMD. The largest observable discrepancy is in the height of the first peak positions of all curves for which the highest peak corresponds to the lowest temperature simulation here (1120 K for LiF and 800 K for FLiBe), decreasing with the increase of temperature. Although at low temperature the peak size is maximized, the radial position of the peak itself experiences no changes across all temperatures, which suggests an approach to crystallization. A similar behavior has been shown for LiF with the Born−Mayer potential, wherein first peak positions near the captured melting point closely correspond with those at much higher temperatures; meanwhile, solid LiF differs in both peak positions and height from its liquid counterpart.[37] Provided, the LiF and FLiBe molten salt data at a constant temperature for training captures the local atomic structures at surrounding temperatures since the structures in the liquid phase are not sensitive to changes across their respective temperature ranges. Additionally, the aforementioned weak dependence of molten salt densities on temperature (*i.e.*, −0.1 g/cm^3 from 800 to 1100 K in FLiBe experiments) also supports the relatively small changes in local structures of the melt. However, we warn others that this behavior may not transfer to other salt mixtures for all temperatures in the liquid phase, and testing for local structures is recommended to discover those unaccounted for at other temperatures especially near the melting point.

3.3. Diffusion Coefficient. In tandem with the structure, the dynamic behavior of molten salts also follows closely with the density and is measured by the diffusion coefficient D. Here, the diffusion coefficients of ions are calculated through the slope of the mean-square displacement *via* the Einstein relation

$$D = \frac{1}{6}\lim_{t\to\infty}\frac{d}{dt}\left[\frac{1}{N}\frac{1}{n_t}\sum_{n_t}^{j=1}\sum_{N}^{i=1}(r_i(t_j + dt) - r_i(t_j))^2\right] \quad (1)$$

where the term inside the brackets is the mean-square displacement (MSD), averaged over atoms N of type i and subsets n_t of time t_j.[19] The diffusion coefficients in Figure 7 increase with the temperature, with lithium-ion diffusion dominating both LiF and FLiBe systems. Additionally, the

https://doi.org/10.1021/acsami.1c17942
ACS Appl. Mater. Interfaces 2021, 13, 55367−55379

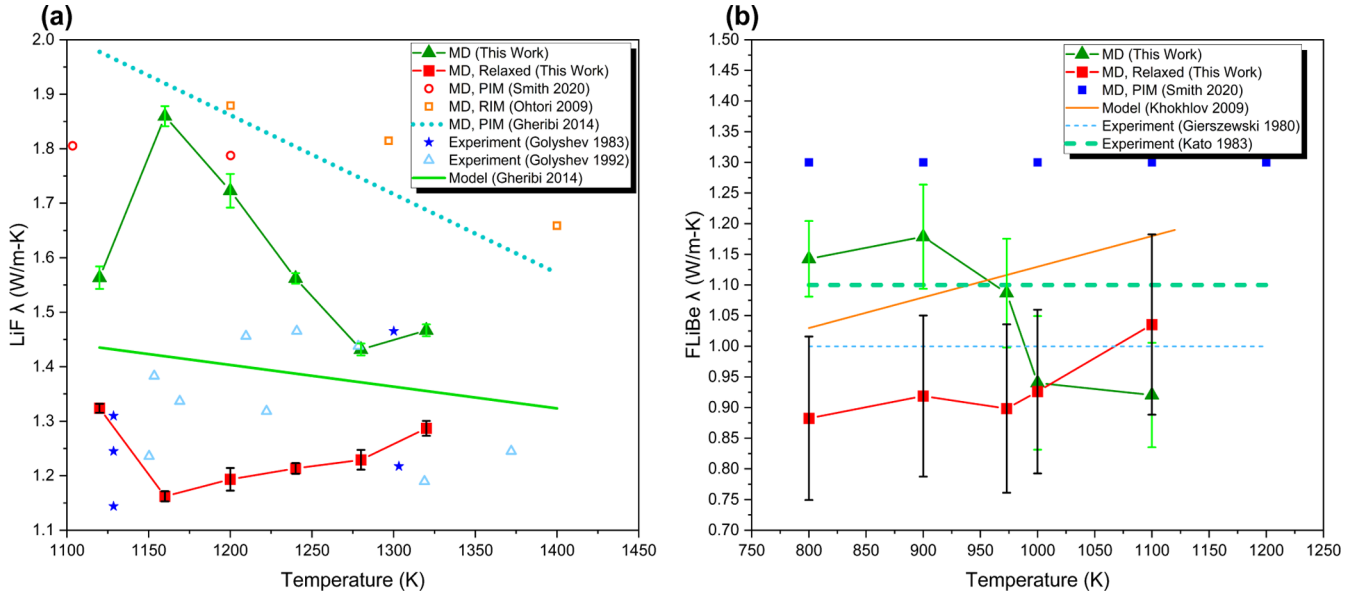

Figure 8. Plots of the thermal conductivity against temperature for LiF and FLiBe above the melting point. (a) In order as shown in the legend, thermal conductivities for LiF at experimental and NPT relaxed volumes are obtained from our work, MD with the polarized ion model,[36] MD with the RIM,[33] fitted line from MD with polarized ion model,[24] experimental results,[41,42] and by a predictive model.[22] (b) Similarly, the thermal conductivities for FLiBe at experimental and NPT relaxed volume are obtained from our work, MD with the polarized ion model,[36] experimental results,[43,44] and by a predictive model.[23] Error bounds are shown in light green for MD simulations at experimental density and black for those at relaxed densities. The heights of the error bounds represent the RMSE about the average thermal conductivity at the tail end of the autocorrelation curves.

fluorine ion diffusion in LiF is significantly more diffusive than that in the FLiBe case, where fluorine diffusion is much closer to the beryllium ion diffusion. The formation of tetrahedral BeF_4^{2-}, $Be_2F_7^{3-}$, and more complex polymer chains may be attributed to the low fluorine and beryllium ion movement due to the increased effective mass of these complexes.[18] Meanwhile, the lithium ion in FLiBe experiences no polymerization and maintains its high mobility. For comparison, the plots also display the diffusion coefficients for the relaxed systems, consistently yielding larger values, albeit the MD temperatures were equivalent to those at experimental volumes. In fact, the LiF and FLiBe diffusion coefficients for the lower density case follow extremely similar trends as those at experimental density, implying no qualitative changes to the structure. This behavior is indicative of a more free-flowing system, where ions and Be−F complexes are less likely to scatter and maintain higher average velocities in the larger simulation cell. Finally, excellent agreement of the DPSE-MD results with other works are shown, although not many points are plotted since the current literature is starved of diffusion data due to the difficulty in measurement.[8]

3.4. Thermal Conductivity. The thermal conductivity λ for ionic liquids is computed in equilibrium molecular dynamics by the Green−Kubo relation through integration of autocorrelation between heat and charge fluxes through the phenomenological coefficients $L_{\alpha\beta}$[38,39]

$$L_{\alpha\beta} = \frac{1}{3k_B V}\int_0^\infty \langle \boldsymbol{j}_\alpha(t)\cdot\boldsymbol{j}_\beta(0)\rangle \mathrm{d}t \tag{2}$$

where thermal conductivity is defined as[36]

$$\lambda = \frac{1}{T^2}\left(L_{ee} - \frac{A}{B}\right) \tag{3}$$

For single-component molten salts, $A = L_{ez}^{\ 2}$ and $B = L_{zz}$, where e and z refer to the heat and charge terms, respectively, and for binary salts, $A = L_{ez_1}^{\ 2}L_{z_2z_2} + L_{ez_2}^{\ 2}L_{z_1z_1} - 2L_{ez_1}L_{ez_2}L_{z_1z_2}$ and $B = L_{z_1z_1}L_{z_2z_2} - L_{z_1z_2}^{\ 2}$. In our simulations, ion 1 is the beryllium ion and ion 2 is the lithium ion. The formulism for charge flux in the binary case used in this work is[16]

$$\boldsymbol{j}_{z_n} = \sum_n (q_n - q_f)^*\boldsymbol{v}_n \tag{4}$$

with n being over all cations in the melt and f as the anion ($q_f = -1$). For improved convergence of the autocorrelation in eq 2, we divide the 1 ns simulation into 1000 1 ps samples and perform a time averaging of the resulting thermal conductivities over these samples.

Because the thermal and electrical conductivity of ionic liquids requires the charge flux of atoms in the simulation cell, we assigned fixed charges corresponding to their chemical element, that is, Li with +1e, F with −1e, and Be with +2e charges. However, the LAMMPS simulations do not consider additional Coulombic forces. This is because DPSE, like other second-generation ML potentials, invokes full electronic interactions including those of Coulombic nature up to the cutoff, but no long-ranged interactions or charge transfer between atoms are considered.[34] Regardless, we obtain agreeable results for the thermal and electronic conductivity in the systems studied here, possibly due to the strongly ionic, well-defined characteristic of the ions in the melt. Future works on MD simulations of molten salts including fixed charges, dynamically altered partial charges, such as those found in the modeling of HfO_2 RRAM cells using the ReaxFF potential,[40] or MLP trained with partial charges from charge equilibration method[34] combined with long-ranged solvers for Coulombic interactions should be considered.

https://doi.org/10.1021/acsami.1c17942
ACS Appl. Mater. Interfaces 2021, 13, 55367−55379

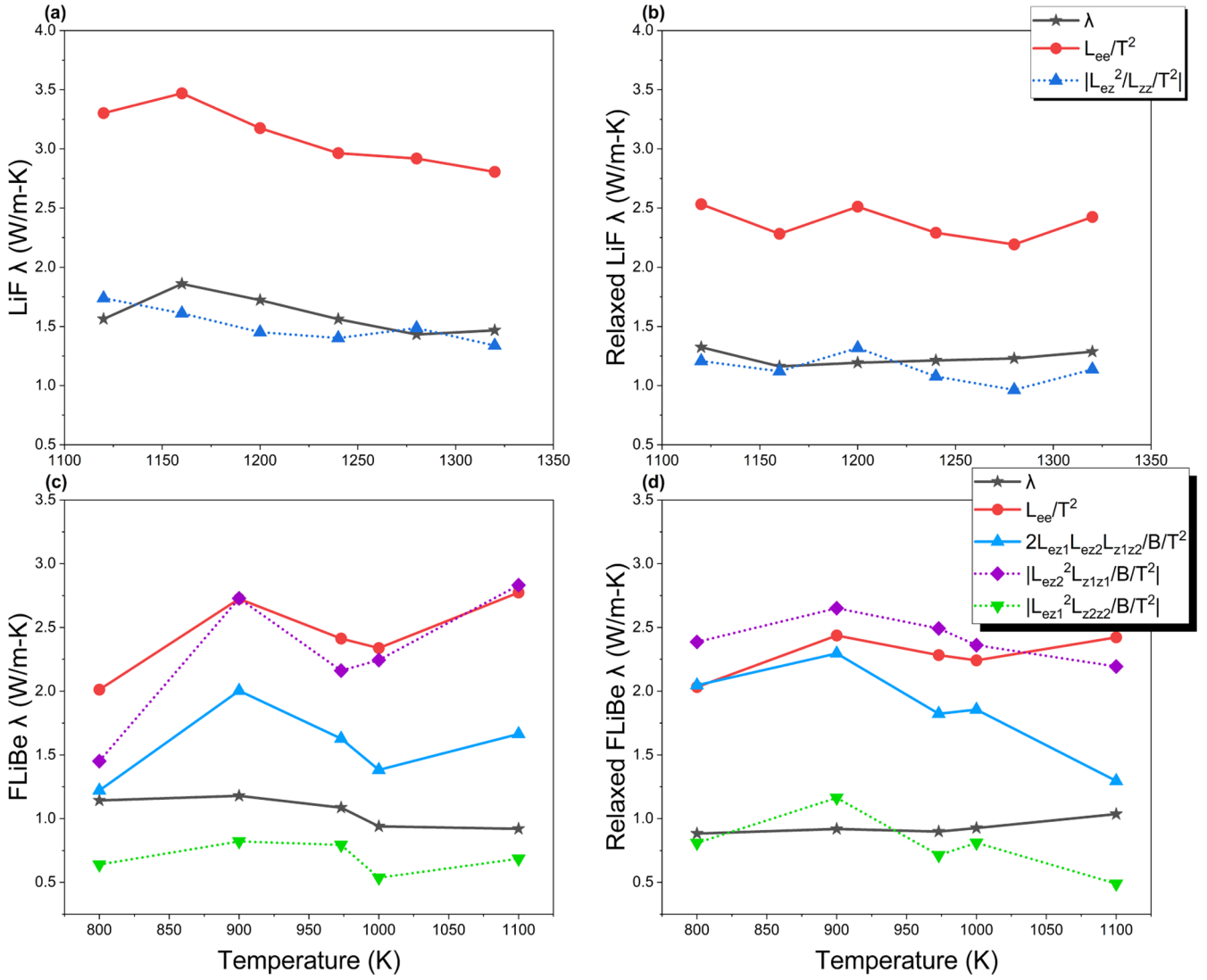

Figure 9. Contributions to the thermal conductivity for (a) LiF, (b) relaxed LiF, (c) FLiBe, and (d) relaxed FLiBe. Solid lines are additive to the thermal conductivity, while dashed lines are subtractive. The total thermal conductivity is also shown.

The thermal conductivities found from DPSE-MD and other works are depicted in Figure 8. For the LiF thermal conductivity, results from the simulations at experimental density fall between those from other MD simulations and experimental results. The thermal conductivity for the relaxed case shows even further improvement, although this may be a coincidence from the increased ion diffusivity in larger volumes. For FLiBe, the agreement with relatively constant thermal conductivity from experiment also matches well with the DPSE results. For the relaxed case, the thermal conductivity remains below that at experimental density until 1100 K, where the thermal conductivity suddenly jumps. Unlike the thermal conductivity for single-component salts, the ratio of determinants A/B for binary salts contains both additive and subtractive terms to the thermal conductivity, and the cause for the behavior becomes non-trivial. We further discuss the difference in thermal conductivity contributions in low- and high-density simulations below.

To understand the effects of phenomenological coefficients in eq 2 on the resulting thermal conductivities of molten salts, their contributions under experimental and MD-relaxed densities are plotted in Figure 9. The construction of thermal conductivity for single salts is subtractive from the pure heat flux term L_{ee} by the cross-correlation charge and heat flux ratio L_{ez}^2/L_{zz}. For LiF in Figures 9a and 8b, the thermal conductivity is approximately halved from that of the heat flux term, yielding a much lower thermal conductivity than the pure heat flux thermal conductivity. On the other hand, for binary salts, the thermal conductivity contributions are no longer purely subtractive but follow a more complex set of contributions by the ratio of determinants A/B. As can be seen from Figures 9c and 8d, while a large portion of the thermal conductivity of FLiBe originates from the heat flux term L_{ee}, an equally large portion is canceled out by the $L_{ez_2}^2 L_{z_1z_1}/B$ term. In our results, we noticed much higher values among the cross-correlation constants for the lithium-ion charge flux with the heat flux L_{ez_2} and to itself $L_{z_2z_2}$, explaining the large conductivity contributions of subtractive $L_{ez_2}^2 L_{z_1z_1}/B$ and additive $2L_{ez_1}L_{ez_2}L_{z_1z_2}/B$. The high contribution to thermal conductivity by lithium may be assigned to its high mobility in FLiBe in comparison to the mobility of fluorine and beryllium ions. In LiF, the high mobility of both lithium and fluorine ions dampens the effect on the subtractive L_{ez}^2/L_{zz} term, unlike in FLiBe where the

https://doi.org/10.1021/acsami.1c17942
ACS Appl. Mater. Interfaces 2021, 13, 55367−55379

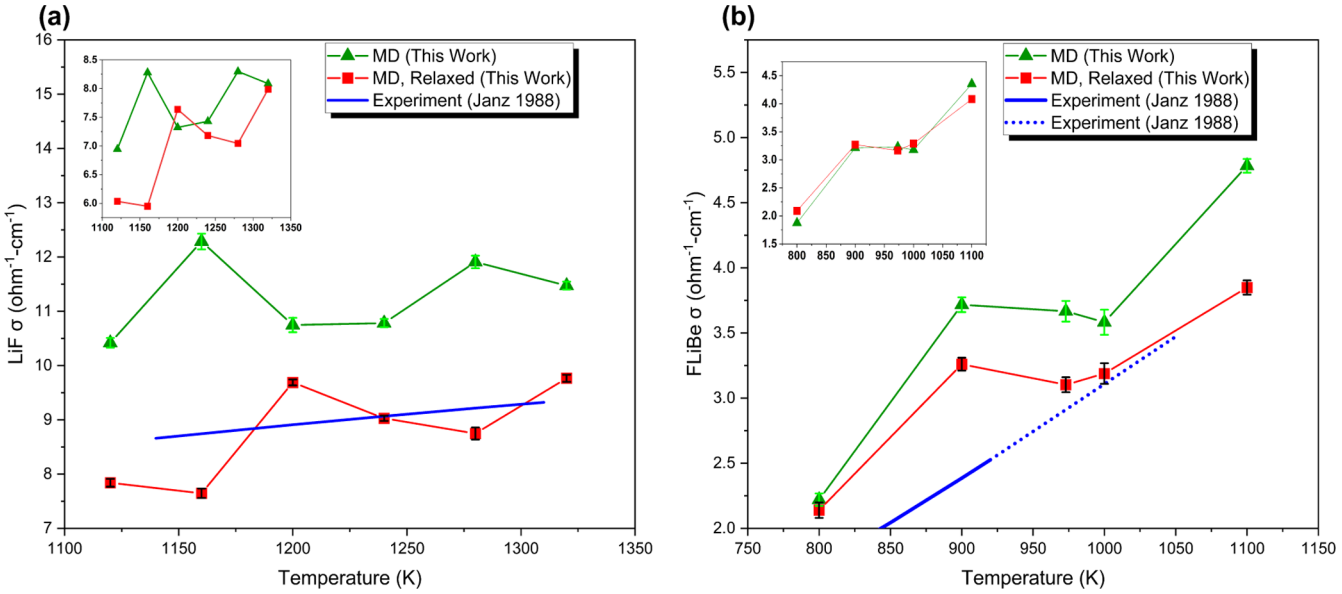

Figure 10. Plots of electrical conductivity against temperature for LiF and FLiBe above the melting point. (a) In order as shown in the legend, electrical conductivities for LiF and (b) FLiBe at experimental and NPT relaxed volumes are obtained from our work. Both plots show experimentally fitted data, where dotted lines represent extrapolated data.[35] (Insets) Extensive electrical conductivity with units 10^{20} ohm^{-1} cm^2. Error bounds are shown in light green for MD simulations at experimental density and black for those at relaxed densities. The heights of the error bounds represent the RMSE about the average electrical conductivity at the tail end of the autocorrelation curves.

heat flux term is essentially canceled out by the existing disparity in ion diffusivity. The lowest contributor to conductivity, $L_{ez_1}{}^2 L_{z_2z_2}/B$, is primarily dictated by the square of the heat charge flux correlation of the beryllium ion $L_{ez_1}{}^2$ and was observed to be about a tenth of the $L_{z_2z_2}$ term. This lowers the effective thermal conductivity reduction of the $L_{ez_1}{}^2 L_{z_2z_2}/B$ term and has the least effect on conductivity. Hence, the term that maintains the conductivity of FLiBe in addition to L_{ee} is $2L_{ez_1}L_{ez_2}L_{z_1z_2}/B$ in which all the heat charge flux terms are weighed similarly (*i.e.*, power to the unity).

To analyze the effects of high (experimental) and low (MD relaxed) density on the resulting thermal conductivity with respect to temperature, their results for LiF and FLiBe are placed together for comparison in Figure 9. In experimental density LiF, the heat flux term L_{ee}/T^2 in Figure 9a greatly influences the thermal conductivity, both experiencing an overall decreasing trend with relatively fixed $L_{ez}{}^2/L_{zz}/T^2$. Indeed, experimental density FLiBe also experiences decreasing thermal conductivity with temperature but is described by a more complex set of coefficients involving several cross-correlation terms with the heat flux, that is, L_{ez_1} and L_{ez_2}, and the behavior is increasingly non-trivial when compared to LiF. From Figure 9c, it can be observed that the decrease is primarily dominated by the increase in the subtractive $L_{ez_2}{}^2 L_{z_1z_1}/B/T^2$ term, most likely attributed by the sudden jump in lithium-ion diffusion after 973 K. Nonetheless, this inverse relation of thermal conductivity with temperature for both single and binary salts is mentioned in previous works and has been attributed to the decreasing density of the melt.[16,33] On the other hand, the thermal conductivities of the melts for the MD relaxed volumes in Figures 9b and 8d are directly proportional to the temperature and deviate from the experimental results despite owning a decreasing density trend as observed in Figure 4. For low-density LiF, both the L_{ee}/T^2 and $L_{ez}{}^2/L_{zz}/T^2$ terms remain relatively constant with their difference, yielding a slight increase in conductivity. Although the L_{ee} term increases in both the low- and high-density simulations, low-density L_{ee} rises more rapidly with temperature than the high-density L_{ee} as seen by the ratio with T^2 and results in a mostly temperature-independent L_{ee}/T^2 contribution. For low-density FLiBe, the increase in thermal conductivity is made possible by a decline in both subtractive $L_{ez_2}{}^2 L_{z_1z_1}/B/T^2$ and $L_{ez_1}{}^2 L_{z_2z_2}/B/T^2$ terms after 900 K, more so than the decline in the additive $2L_{ez_1}L_{ez_2}L_{z_1z_2}/B/T^2$ term. The drop in all the three terms with temperature which involve charge−charge and charge−heat cross-correlations is again most likely due to the weaker scaling with T^2 for the low-density case. We note that despite division by $B = L_{z_1z_1}L_{z_2z_2} - L_{z_1z_2}{}^2$, both high-density and low-density simulations owned matching values of B and contributed little to the mentioned trends. In summary, we have shown how the simulated density affects thermal conductivity behavior against temperature, reinforcing our earlier statement to accurately capture the density before approaching other properties.

3.5. Electrical Conductivity. The electrical conductivity σ in MD simulations may be found through the MSD of charges in the melt, the Nernst−Einstein approximation, or through the Green−Kubo formalism.[12,38] Since the Green−Kubo thermal conductivity for ionic liquids requires the charge correlation term L_{zz}, the electrical conductivity is readily available by dividing by the temperature. Note that the L_{zz} term is found through the charge flux of all atoms in the system; hence, the charge flux for single-component salts is applied to the electrical conductivity for FLiBe. For improved convergence of the autocorrelation, we divide the 1 ns into 1000 1 ps samples and perform time averaging of the resulting electrical conductivity. The results for LiF and FLiBe electrical conductivity are provided in Figure 10 with fitted experimental results from Janz et al.[35] Here, the electrical conductivity

https://doi.org/10.1021/acsami.1c17942
ACS Appl. Mater. Interfaces 2021, 13, 55367−55379

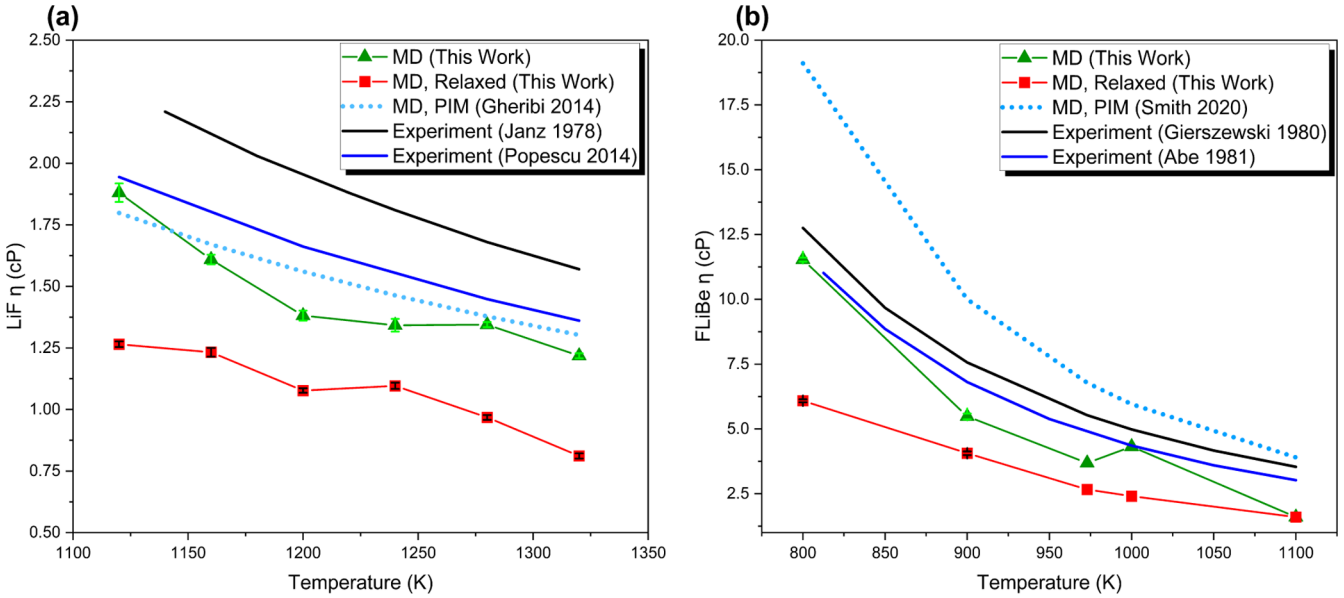

Figure 11. Plots of viscosity against temperature for LiF and FLiBe above the melting point. (a) In order as shown in the legend, viscosities for LiF at experimental and NPT relaxed volumes are obtained from our work, MD with the polarized ion model,[24] and experiments.[46,47] (b) Similarly, viscosities for FLiBe at experimental and NPT relaxed volumes are obtained from our work, MD with the polarized ion model,[36] and experiments.[43,48] Error bounds are shown in light green for MD simulations at experimental density and black for those at relaxed densities. Those with limited height are omitted for visual purposes. The heights of the error bounds represent the RMSE about the average viscosity at the tail end of the autocorrelation curves.

matches well with the experiment following an increasing trend against temperature. Interestingly, the results from low-density simulations yield lower electrical conductivity values despite owning higher ionic mobility. The difference in the electrical conductivity is primarily attributed to the division by the volume in the L_{zz} term from eq 2. The insets of Figure 10 contain the electrical conductivity multiplied by the cell volume for the extensive electrical conductivity, where an improved agreement between the relaxed and experimental density simulations is observed. For LiF, a slight disagreement remains; although based on the fluctuations of the electrical conductivity, we attribute the uncertainty toward the Green−Kubo MD. For FLiBe, an improved overlap in the extensive electrical conductivity is observed. Based on these results, the electrical conductivity owns a strong dependence on density.

3.6. Viscosity. The shear viscosity η is found similarly to the Green−Kubo thermal conductivity[45]

$$\eta = \frac{V}{k_B T}\int_0^\infty \langle P_{\alpha\beta}(t)\cdot P_{\alpha\beta}(0)\rangle \mathrm{d}t \tag{5}$$

where $P_{\alpha\beta}$ represents the off-diagonal terms in the pressure tensor during MD. For improved statistics, the viscosity is averaged over P_{xy}, P_{xz}, and P_{yz} terms. Optionally, the viscosity may also be averaged over P_{xx-yy} and $P_{2zz-xx-yy}$, but the first three terms were sufficient for convergence of the autocorrelation function.[24] In addition, due to the Arrhenius relation of viscosity to temperature, the convergence of the autocorrelation in eq 5 requires variable autocorrelation times for the time averaging over the span of the 1 ns simulation time. Specifically, for convergence of viscosity plateaus regardless of the simulated experimental or relaxed densities, the autocorrelation times for LiF were 5 ps for all simulated temperatures, while those of FLiBe were 15, 15, 10, 5, and 5 ps in order of increasing temperatures. As can be seen in Figure 11, the viscosity of LiF and FLiBe at experimental densities matches well with experimental works, while those found from relaxed supercells own significantly lower viscosity. In comparison to the PIM model, the LiF viscosity agrees well with other works, while the FLiBe viscosity underestimates the experimental viscosities with PIM overestimating by a similar magnitude. It is well known that the viscosity is a difficult property to predict from MD simulations due to the required long simulation times for converged autocorrelation in eq 5, and here, the relatively short 1 ns simulation time is a potential source of error.[8,36] Nonetheless, the agreement with experimental trends is acceptable with matching errors from those of other MD works. Other works have shown that the viscosity owns an inverse relationship with the diffusion coefficient,[37] and the diffusion coefficient increases with decreased density as previously observed in Figure 7. For example, the higher ionic mobility in the relaxed supercell is consistent with the lowered viscosity, further increasing the ionic mobility and decreasing the viscosity from expansion due to the temperature. As such, the viscosity is directly proportional to the density of molten salts as observed by its decrease with increasing volume and temperature.

4. CONCLUSIONS

An investigation on the thermodynamic and transport properties of molten salts LiF and FLiBe is performed, where flexible and rapid MLPs are fitted with DFT data without the need of pre-existing physical models. The matching of local structures with AIMD and diffusion coefficients with experiment displays the excellent ability of the MLPs to reproduce complex energy surfaces and realistic dynamics. With the linear scaling of Deep Potential Smooth Edition (DPSE) neural networks, we explored the dynamics of molten salts using large supercells through MD with DFT accuracy. Due to the difficulty of evaluating dynamic properties in experiments, the diffusion coefficients, thermal conductivity,

https://doi.org/10.1021/acsami.1c17942
ACS Appl. Mater. Interfaces 2021, 13, 55367−55379

electrical conductivity, and viscosity of LiF and FLiBe were predicted within the acceptable accuracy of experiments and other works using MD. Although the density of molten salts only has reasonable agreement with experimental results, the resulting densities are linked to the lack of dispersion relations in the training data and match previous works excluding these interactions.[17,21] In future studies, dispersion considerations in DFT packages will be studied to consider polarization in the training data and improve the atomic interactions in molten salt MLPs. Inclusion of long-ranged interactions beyond the cutoff of DPMD may also improve the resulting density.

Here, we conclude this work with a perspective on the future of atomic molten salt modeling. With the massive design space of molten salts, developing parameterized potentials, for example, PIM potentials for all possible compositions would take much effort and time. Instead, the "hands-free" approach of MLPs is crux for the development of general potentials that can simultaneously cover a wide range of molten salt compositions and temperatures, essentially spanning across the periodic table. The multi-dimensional, non-linear nature of MLPs allows for a higher degree of transferability that is cut short by the limited flexibility of parametric potentials. However, one of the main limitations of recent MLPs is the exponential scaling of model parameters with the number of elements. For example, the popular high-dimensional neural network potential (HDNNP) requires N radial and $N(N + 1)$ angular symmetry functions for each element-specific network, which can quickly slow down both training and the evaluation of structures with increasing elements N.[49] Although the DPSE potential used in this paper necessitates no user-specified descriptors such as symmetry functions, the model still requires N fitting networks with N^2 embedding networks and is increasingly more time-consuming during training and evaluation steps for large number of elements.[28,50] Furthermore, descriptors should be designed in such a way that any number of elements may be added without needing to reconstruct and train the model from scratch. Generating such descriptors from data spanning many elements could enable a reduction in, for example, network complexity if a new element only changes the NN input numerically rather than the shape/size of networks or improve training speeds if only one network can well describe both input atomic positions and species. This opens the opportunity to develop potentials without the need to re-fit *ab initio* data when new chemical element is introduced, allowing for MLPs to *grow* rather remain limited to a fixed set of chemistries. An example would be to add chromium impurity to an existing trained FLiBe MLP. Another difficulty for general potential development is the generation of sufficient structures for training. Because molten salts contain local atomic structures characteristic of the composition and concentration of end members, it is critical to capture these local structures while requiring minimal lengthy DFT evaluations. The generation of structures purely *via* AIMD is excessively expensive, considering that many structures encountered in MD may be redundant or lacking distinctive features for MLP training. Therefore, more effective sampling methods are needed to speed up this process. In addition, the transferability of our model to other compositions is tested here on FLiBe, with increasingly higher disagreement to the linearly decreasing temperature relation of the density as one departs from 33% BeF_2. Despite this, we observe that the resulting simulations are stable and their densities are comparable to the composition of the training set, implying some degree of transferability. We expect an improvement in the model with further training on other compositions; however, we leave this for future work due to the expensive nature of AIMD simulations. On the other hand, active learning techniques offer the opportunity to generate data efficiently by sampling new configurations with the MLP itself, requiring DFT only when the model recognizes a poorly represented atomic configuration. The active learning approach recently presented by Zhang et al. addresses the bottleneck of dataset generation by exploration and labeling of configurations through DPSE-MD, cutting down the required number of DFT evaluations to 0.0044% of the total number of configurations explored.[51] Therefore, active learning can significantly improve the search for poorly represented local structures in molten salts varying with respect to temperature and composition while minimizing the needed DFT to generate the training set. Essentially, the development of MLPs with improved elemental scaling and minimal DFT calculations is keystone for modeling a wide range of molten salts for rapid database development. Currently, we are working on a modification of deep learning potentials that changes how the model distinguishes elements with improved scaling in model complexity for application on molten salts and existing large databases containing materials such as ceramics and semiconductors.

AUTHOR INFORMATION

Corresponding Author

Alejandro Rodriguez − *Department of Mechanical Engineering, University of South Carolina, Columbia, South Carolina 29208, United States;* orcid.org/0000-0001-6219-382X; Email: alejandroadr@outlook.com

Authors

Stephen Lam − *Department of Chemical Engineering, University of Massachusetts Lowell, Lowell, Massachusetts 01854, United States;* orcid.org/0000-0002-7683-1201

Ming Hu − *Department of Mechanical Engineering, University of South Carolina, Columbia, South Carolina 29208, United States;* orcid.org/0000-0002-8209-0139

Complete contact information is available at: https://pubs.acs.org/10.1021/acsami.1c17942

Notes

The authors declare no competing financial interest.

ACKNOWLEDGMENTS

This material is based upon work supported under a Department of Energy, Office of Nuclear Energy, Integrated University Program Graduate Fellowship (IUP), and Nuclear Energy University Program. A.R. is financially supported by the IUP under award no. DE-NE-0000095. S.L. is supported by award no. DE-NE0009204. Research reported in this publication was supported in part by the NSF (award no. 2030128).

REFERENCES

(1) *A Technology Roadmap for Generation IV Nuclear Energy Systems*. Nuclear Energy Research Advisory Committee Generation IV International Forum, 2014, GIF--002--00.

(2) Andrew, C. K. A. *Comparison of Advanced Nuclear Technologies*; Columbia SIPA, 2017; p 112.

(3) Heuer, D.; Merle-Lucotte, E.; Allibert, M.; Brovchenko, M.; Ghetta, V.; Rubiolo, P. Towards the Thorium Fuel Cycle with Molten Salt Fast Reactors. *Ann. Nucl. Energy* **2014**, *64*, 421−429.
(4) Elsheikh, B. M. Safety Assessment of Molten Salt Reactors in Comparison with Light Water Reactors. *J. Radiat. Res. Appl. Sci.* **2013**, *6*, 63−70.
(5) Carlson, K.; Gardner, L.; Moon, J.; Riley, B.; Amoroso, J.; Chidambaram, D. Molten Salt Reactors and Electrochemical Reprocessing: Synthesis and Chemical Durability of Potential Waste Forms for Metal and Salt Waste Streams. *Int. Mater. Rev.* **2021**, *66*, 339−363.
(6) Yoshioka, R.; Kinoshita, M.; Scott, I. Materials. *Molten Salt Reactors and Thorium Energy*; Woodhead Publishing, 2017.
(7) *Molten Salt Chemistry Workshop. Innovation Approaches to Accelerate Molten Salt Reactor Development and Deployment*; Oak Ridge National Laboratory. Technology and Applied R&D; 2017.
(8) Dai, J.-X.; Zhang, W.; Ren, C.-L.; Guo, X.-J. Prediction of Dynamics Properties of ThF4-Based Fluoride Molten Salts by Molecular Dynamic Simulation. *J. Mol. Liq.* **2020**, *318*, 114059.
(9) Cadwallader, L. C.; Longhurst, G. R. *Flibe Use in Fusion Reactors: An Initial Safety Assessment*. Idaho National Laboratory, 1999. No. March, 1−25.
(10) Dewan, L. C.; Simon, C.; Madden, P. A.; Hobbs, L. W.; Salanne, M. Molecular Dynamics Simulation of the Thermodynamic and Transport Properties of the Molten Salt Fast Reactor Fuel LiF-ThF4. *J. Nucl. Mater.* **2013**, *434*, 322−327.
(11) Salanne, M.; Rotenberg, B.; Jahn, S.; Vuilleumier, R.; Simon, C.; Madden, P. A. Including Many-Body Effects in Models for Ionic Liquids. *Theor. Chem. Acc.* **2012**, *131*, 1−16.
(12) Salanne, M.; Simon, C.; Turq, P.; Heaton, R. J.; Madden, P. A. A First-Principles Description of Liquid BeF2 and Its Mixtures with LiF: 2. Network Formation in LiF−BeF2. *J. Phys. Chem. B* **2006**, *110*, 11461−11467.
(13) Sarou-Kanian, V.; Rollet, A.-L.; Salanne, M.; Simon, C.; Bessada, C.; Madden, P. A. Diffusion Coefficients and Local Structure in Basic Molten Fluorides: In Situ NMR Measurements and Molecular Dynamics Simulations. *Phys. Chem. Chem. Phys.* **2009**, *11*, 11501−11506.
(14) Ishii, Y.; Kasai, S.; Salanne, M.; Ohtori, N. Transport Coefficients and the Stokes-Einstein Relation in Molten Alkali Halides with Polarisable Ion Model. *Mol. Phys.* **2015**, *113*, 2442−2450.
(15) Salanne, M.; Madden, P. A. Polarization Effects in Ionic Solids and Melts. *Mol. Phys.* **2011**, *109*, 2299−2315.
(16) Ishii, Y.; Sato, K.; Salanne, M.; Madden, P. A.; Ohtori, N. Thermal Conductivity of Molten Alkali Metal Fluorides (LiF, NaF, KF) and Their Mixtures. *J. Phys. Chem. B* **2014**, *118*, 3385−3391.
(17) Nam, H. O.; Bengtson, A.; Vörtler, K.; Saha, S.; Sakidja, R.; Morgan, D. First-Principles Molecular Dynamics Modeling of the Molten Fluoride Salt with Cr Solute. *J. Nucl. Mater.* **2014**, *449*, 148−157.
(18) Lam, S. T.; Li, Q.-J.; Mailoa, J.; Forsberg, C.; Ballinger, R.; Li, J. The Impact of Hydrogen Valence on Its Bonding and Transport in Molten Fluoride Salts. *J. Mater. Chem. A* **2021**, *9*, 1784−1794.
(19) Lam, S. T.; Li, Q.-J.; Ballinger, R.; Forsberg, C.; Li, J. Modeling LiF and FLiBe Molten Salts with Robust Neural Network Interatomic Potential. *ACS Appl. Mater. Interfaces* **2021**, *13*, 24582.
(20) Zhang, L.; Han, J.; Wang, H.; Car, R.; Weinan, E. Deep Potential Molecular Dynamics: A Scalable Model with the Accuracy of Quantum Mechanics. *Phys. Rev. Lett.* **2018**, *120*, 1−6.
(21) Jabes, B. S.; Agarwal, M.; Chakravarty, C. Structure and transport properties of LiF-BeF2 mixtures: Comparison of rigid and polarizable ion potentials#. *J. Chem. Sci.* **2012**, *124*, 261−269.
(22) Gheribi, A. E.; Torres, J. A.; Chartrand, P. Recommended Values for the Thermal Conductivity of Molten Salts between the Melting and Boiling Points. *Sol. Energy Mater. Sol. Cells* **2014**, *126*, 11−25.
(23) Khokhlov, V.; Ignatiev, V.; Afonichkin, V. Evaluating Physical Properties of Molten Salt Reactor Fluoride Mixtures. *J. Fluorine Chem.* **2009**, *130*, 30−37.
(24) Gheribi, A. E.; Corradini, D.; Dewan, L.; Chartrand, P.; Simon, C.; Madden, P. A.; Salanne, M. Prediction of the Thermophysical Properties of Molten Salt Fast Reactor Fuel from First-Principles. *Mol. Phys.* **2014**, *112*, 1305−1312.
(25) Wang, J.; Sun, Z.; Lu, G.; Yu, J. Molecular Dynamics Simulations of the Local Structures and Transport Coefficients of Molten Alkali Chlorides. *J. Phys. Chem. B* **2014**, *118*, 10196−10206.
(26) Wang, H.; Zhang, L.; Han, J.; E, W. DeePMD-Kit: A Deep Learning Package for Many-Body Potential Energy Representation and Molecular Dynamics. *Comput. Phys. Commun.* **2018**, *228*, 178−184.
(27) Abadi, M.; Barham, P.; Chen, J.; Chen, Z.; Davis, A.; Dean, J.; Devin, M.; Ghemawat, S.; Irving, G.; Isard, M.; Kudlur, M.; Levenberg, J.; Monga, R.; Moore, S.; Murray, D. G.; Steiner, B.; Tucker, P.; Vasudevan, V.; Warden, P.; Wicke, M.; Yu, Y.; Zheng, X. *TensorFlow: A System for Large-Scale Machine Learning*. 12th {USENIX} Symposium On Operating Systems Design And Implementation ({OSDI} 16), 2016; Vol. *2016*, pp 265−283.
(28) Zhang, L.; Han, J.; Wang, H.; Saidi, W. A.; Car, R.; Weinan, E. End-to-End Symmetry Preserving Inter-Atomic Potential Energy Model for Finite and Extended Systems. **2018**, arXiv:1805.09003.
(29) Plimpton, S. Fast Parallel Algorithms for Short-Range Molecular Dynamics. *J. Comput. Phys.* **1995**, *117*, 1−19.
(30) Adams, D. J.; McDonald, I. R. Rigid-ion models of the interionic potential in the alkali halides. *J. Phys. C: Solid State Phys.* **1974**, *7*, 2761−2775.
(31) Wang, S.; Luo, H.; Deng, H.; Xiao, S.; Hu, W. A molecular dynamics study of the transport properties of LiF-BeF 2 -ThF 4 molten salt. *J. Mol. Liq.* **2017**, *234*, 220−226.
(32) Rodriguez, A.; Liu, Y.; Hu, M. Spatial Density Neural Network Force Fields with First-Principles Level Accuracy and Application to Thermal Transport. *Phys. Rev. B* **2020**, *102*, 35203.
(33) Ohtori, N.; Oono, T.; Takase, K. Thermal Conductivity of Molten Alkali Halides: Temperature and Density Dependence. *J. Chem. Phys.* **2009**, *130*, 044505.
(34) Ko, T. W.; Finkler, J. A.; Goedecker, S.; Behler, J. A Fourth-Generation High-Dimensional Neural Network Potential with Accurate Electrostatics Including Non-Local Charge Transfer. *Nat. Commun.* **2021**, *12*, 1−11.
(35) Janz, G. Thermodynamic and Transport Properties for Molten Salts Correlation Equations for Critically Evaluated Density, Surface Tension, Electrical Conductance, and Viscosity Data. *J. Phys. Chem. Ref. Data* **1988**, *17*, 311.
(36) Smith, A. L.; Capelli, E.; Konings, R. J. M.; Gheribi, A. E. A New Approach for Coupled Modelling of the Structural and Thermo-Physical Properties of Molten Salts. Case of a Polymeric Liquid LiF-BeF2. *J. Mol. Liq.* **2020**, *299*, 112165.
(37) Luo, H.; Xiao, S.; Wang, S.; Huai, P.; Deng, H.; Hu, W. Molecular Dynamics Simulation of Diffusion and Viscosity of Liquid Lithium Fluoride. *Comput. Mater. Sci.* **2016**, *111*, 203−208.
(38) Galamba, N.; Nieto de Castro, C. A.; Ely, J. F. Thermal Conductivity of Molten Alkali Halides from Equilibrium Molecular Dynamics Simulations. *J. Chem. Phys.* **2004**, *120*, 8676−8682.
(39) Galamba, N.; Nieto de Castro, C. A.; Ely, J. F. Equilibrium and Nonequilibrium Molecular Dynamics Simulations of the Thermal Conductivity of Molten Alkali Halides. *J. Chem. Phys.* **2007**, *126*, 204511.
(40) Urquiza, M. L.; Islam, M. M.; Van Duin, A. C. T.; Cartoixà, X.; Strachan, A. Atomistic Insights on the Full Operation Cycle of a HfO2-Based Resistive Random Access Memory Cell from Molecular Dynamics. *ACS Nano* **2021**, *15*, 12945−12954.
(41) Golyshev, V. D.; Gonik, M. A. High-Temperature Thermo-physical Properties of Non-Scattering Semitransparent Materials III: Thermal Conductivity of Melts. *High Temp. - High Press.* **1992**, *24*, 677−688.

https://doi.org/10.1021/acsami.1c17942
ACS Appl. Mater. Interfaces 2021, 13, 55367−55379

(42) Golyshev, V. D.; Gonik, M. A.; Petrov, V. A.; Putilin, Y. M. *Teplofiz. Vysok. Temp.* **1983**, *21*, 899−903.
(43) Gierszewski, P.; Mikic, B.; Trodreas, N. *Properties Correlations for Li Na He FLIBE and Water in Fusion Reactor Applications*; Massachusetts Institute of Technology, 1980.
(44) Kato, Y.; Furukawa, K.; Araki, N.; Kobayasi, K. Thermal Diffusivity Measurement of Molten Salts by Use of a Simple Ceramic Cell. *High Temp. - High Press* **1983**, *15*, 191−198.
(45) Zhang, Y.; Otani, A.; Maginn, E. J. Reliable Viscosity Calculation from Equilibrium Molecular Dynamics Simulations: A Time Decomposition Method. *J. Chem. Theory Comput.* **2015**, *11*, 3537−3546.
(46) Janz, G. J.; Allen, C. B.; Downey, J. R., Jr.; Tomkins, R. P. T. *Physical Properties Data Compilations Relevant to Energy Storage*; NSRDS, 1978.
(47) Popescu, A.-M.; Constantin, V. Viscosity of Alkali Fluoride Ionic Melts at Temperatures up to 373.15 K above Melting Points. *Chem. Eng. Commun.* **2015**, *202*, 1703−1710.
(48) Abe, Y.; Kosugiyama, O.; Nagashima, A. Viscosity of LiF-BeF2 Eutectic Mixture (XBeF2 = 0.328) and LiF Single Salt at Elevated Temperatures. *J. Nucl. Mater.* **1981**, *99*, 173−183.
(49) Gastegger, M.; Schwiedrzik, L.; Bittermann, M.; Berzsenyi, F.; Marquetand, P. wACSF-Weighted atom-centered symmetry functions as descriptors in machine learning potentials. *J. Chem. Phys.* **2018**, *148*, 241709.
(50) Lu, D.; Wang, H.; Chen, M.; Lin, L.; Car, R.; E, W.; Jia, W.; Zhang, L. 86 PFLOPS Deep Potential Molecular Dynamics Simulation of 100 Million Atoms with Ab Initio Accuracy. *Comput. Phys. Commun.* **2021**, *259*, 107624.
(51) Zhang, L.; Lin, D.-Y.; Wang, H.; Car, R.; Weinan, E. Active Learning of Uniformly Accurate Interatomic Potentials for Materials Simulation. *Phys. Rev. Mater.* **2019**, *3*, 23804.

https://doi.org/10.1021/acsami.1c17942
ACS Appl. Mater. Interfaces 2021, 13, 55367−55379